19th AIAA Computational Fluid Dynamics
22 - 25 June 2009, San Antonio, Texas

AIAA Paper 2009-3880
AIAA 2009-3880

A Hybrid Cartesian-Body Fitted Grid Approach for Simulation of Flows in Complex Geometries

Xiangying Chen[*] and Ge-Cheng Zha[†]
Dept. of Mechanical and Aerospace Engineering
University of Miami
Coral Gables, Florida 33124

Abstract

A novel approach of automated hybrid Cartesian-body fitted grid (HCBFG) for simulations of fluid flows in complex geometries is suggested. Based on a Cartesian background grid, the new approach automatically searches a near wall boundary(NWB) at any instant when a geometry is given. Within the NWB, a body-fitted mesh is generated using an efficient algebraic method with the skew angle between any two mesh lines guaranteed between 45° and 135°. This is attributed to the fact that only the mesh lines tangential to the solid surface needs to be generated. The mesh lines in the other two directions are from the background Cartesian grid. Outside of the NWB, the Cartesian grid is used. On the NWB, the grid points are one-to-one connected with the Cartesian grid. Hence, a consistent discretization scheme for structured grid can be used with no interpolation needed at the NWB. The fully conservative flux calculation can be achieved.

This new approach has the advantages of the Chimera grid and Cartesian grid methods to treat complex or moving geometry, but overcomes the drawbacks of those methods requiring interpolation on the different mesh boundaries. Benefited from the HCBFG, all the rigorous numerical techniques developed for body-fitted grid, which are essential to achieve high order accuracy, can be used. The mesh size of the proposed hybrid grid approach will also be substantially smaller than that of a Cartesian grid method or unstructured grids since a highly stretched grid can be used near walls. This new approach may open a door to a new class of CFD technique for efficiently and accurately simulating steady and unsteady flows, furthermore, solving moving grid and fluid-structural interaction problems with complex geometries. This paper presents several examples of the HCBFG for representative geometries. The transonic RAE2822 airfoil is calculated using an implicit line Gauss-Seidel iteration to demonstrate the feasibility of the method.

1 Introduction

In a finite differencing or finite volume simulation, the body-fitted curvilinear structured grid methodology transforms the flow governing equations from a physical domain (x, y, z, t) to a computational domain (ξ, η, ζ, τ), which provides the most rigorous way to achieve high order accuracy[1, 2, 3, 4, 5, 6, 7]. One advantage of a body-fitted structured grid is that the numerical accuracy based on Taylor's series expansion is satisfied since uniform discretization grid spacing is achieved in the computational space. For moving grid problems, the moving grid velocity is naturally included in the transformation and the geometry conservation law can be accurately enforced. One very useful feature of structured grid is that the grid spacing normal to a wall boundary can be highly stretched. A grid aspect ratio up to 1000 or higher is commonly used. This feature is very important to efficiently resolve high Reynolds number flows with wall boundary layers.

---

[*] Research Associate Professor
[†] Associate Professor

The grid size of a structured body-fitted grid can be estimated as the following: for a 3D problem with characteristic length scale of L and boundary layer thickness of δ, the grid size required by a structured grid is $(L/\Delta_t)(\delta/\Delta_n)(aL/\Delta_s)$, where Δ_t, Δ_n and Δ_s are the averaged grid spacings in the tangential, normal and spanwise directions to the wall surface, a is the ratio of the transverse length to the characteristic length.

In principle, the body-fitted structured grid methodology can treat any flow problems. In reality however, it could be difficult to generate high quality mesh for a complex geometry, especially in an automated and efficient way. To overcome the difficulties of structured grid generation of a complex geometry, the Chimera overset grids method was developed by Steger et al [8, 9, 10] to decompose a mesh system of a complex geometry to multiple simpler geometry components which are easier to be dealt with by a structured grid generator. The Chimera scheme allows a system of relatively simple grids to be combined into a composite grid. One advantage of Chimera grid is that all the high order accuracy numerical algorithms developed for the body-fitted structured grids can be directly used[11, 12].

The drawbacks of using Chimera overset grids include having to interpolate data along an irregular boundary. Such interpolation makes the enforcement of global flux conservation very difficult if not impossible. In addition, the bookkeeping can be especially complex if more than two grids overlapping each other. Special software such as PEGSUS[13] has been developed to interconnect the overset grids, create proper hole regions, define interface and hole boundaries, and determine the interpolation stencils for properly transmitting information between overset grids. Overall, the mesh generation of a complex geometry system using Chimera grid approach can be very time consuming.

In parallel to the Chimera overset grid, the numerical algorithms based on unstructured grids have been developed to tackle complex geometry. Recently, there have been some efforts to solve moving-body problems with unstructured overset grid and deforming unstructured grid approaches[14, 15, 16]. However, for unstructured overset grid methods, handling the failed interpolation grid points is still not well resolved. On the other hand, large deformation and excessive computational requirements are issues that still need to be resolved for deforming unstructured grid approaches. In addition, the high order schemes of unstructured grids for 3D Navier-Stokes equation such as the discontinuous Galerkin method [17, 18] and High-Order Spectral Volume Method [19, 20] are still immature and the application to fluid-structural interaction is difficult. The other drawback of the unstructured grid is that the efficient line relaxation iteration of structured grids can not be used and an implicit unstructured method has to rely on the less efficient point relaxation method. Furthermore, an unstructured grid flow solver usually can not tolerate high aspect ratio grid like a structured grid flow solver. The mesh size in the near wall region hence will be significantly larger than a structured grid. For high Reynolds number flows of military aircraft, it is questionable if a unstructured grid CFD solver with triangle or tetrahedral mesh cells is suitable to accurately resolve wall boundary layers.

Different from the body-fitted structured or unstructured grid methodology, the numerical algorithms using non-boundary conforming Cartesian grids (CG) to treat complex geometry have been actively developed. These methods may be classified to two categories[21]: 1) Immersed boundary (IB) methods enforcing wall conditions indirectly by using forcing functions in the flow governing equations[22, 23, 24, 25, 26], and 2) Cartesian cut-cell methods based on the construction of irregular body-fitted cells near solid surfaces[27, 28, 29, 30, 31]. Berger et al.[32] developed an adaptive mesh refinement scheme incorporated in a Cartesian grid embedded boundary method. Later, they developed a high-resolution rotated grid h-box method based their Cartesian grid approach [33, 34].

The Cartesian grid IB methods have attracted increased interest recently due to their simplicity of grid generation for complex geometry. However, the following three disadvantages may restrict their application: 1) The IB methods require an enormous grid size for high Reynolds number flows.

The grid is not stretched nor body-fitted near wall surfaces, and it hence requires an extremely large grid size if a high Reynolds number turbulent wall boundary layer flow is simulated, in particular if the detailed wall boundary layer eddy structures are of interest. For a 3D high Reynolds number turbulent flow, the grid size ratio of a Cartesian grid to a body-fitted curvilinear structured grid scales with $Re^{1.5}$[21]. This raises a serious question if the Cartesian grid IB method is feasible at all to simulate high Reynolds number flows. 2)the Cartesian grid IB method is difficult to enforce flux conservation and hence solution accuracy due to the required interpolation. 3)the forcing function treatment so far can only achieve 2nd order accuracy in the boundary, which may limit the accuracy of the flow solution using high order accuracy numerical schemes for LES, DES, and DNS.

The Cartesian grid cut cell method is able to impose accurate wall boundary conditions. However, it has the same problem as the IB method that needs an extremely large mesh size to resolve 3D high Reynolds number turbulent wall boundary layers. In addition, the discretization scheme inside the cut cells is usually different from the one used for the main flow domain. It hence also requires interpolation and extrapolation, and will then lose flux conservation and accuracy. The application of a cut cell method to 3D problems is also not straightforward.

In conclusion, the body-fitted structured grid has the advantage to resolve high Reynolds number wall boundary layer by using highly stretched grid in the direction normal to the wall surface, but has the difficulty to generate the mesh for a complex geometry system in an efficient and automated fashion. The Cartesian and unstructured (triangle elements) grids have the flexibility to deal with a complex geometry, but have the difficulty in resolving the high gradient wall boundary layers due to non-stretched grids.

As mentioned previously, Cartesian grid requires a large grid size for a high Reynolds number flow simulation. To further improve the present approach, it is necessary to use coarse grids in the flow farfield where flow variable gradients are small. The conservation between the two different mesh systems can be achieved by using the conservative interface procedures. One of early efforts in that area was made by Berger [35]. In [35], a procedure was proposed to derive conservative difference approximations at grid interfaces for two grids overlap each other.

The new approach of hybrid Cartesian-body fitted grid (HCBFG) suggested in this paper is aimed at combining the advantage of the body-fitted structured grid in resolving high gradient wall boundary layers and the advantage of the Cartesian grid in handling complex geometries. Based on a Cartesian background grid, the new approach automatically searches a near wall boundary(NWB) at any instant when a boundary is given. Within the NWB, a body-fitted mesh is generated using an efficient algebraic method with the skew angle between any two mesh lines guaranteed between 45° and 135°. Outside of the NWB, the Cartesian grid is used. On the NWB, the grid points are one-to-one connected with the Cartesian grid. Hence, a consistent discretization scheme for structured grid can be used with no interpolation needed at the NWB. The fully conservative flux calculation can be achieved. The detailed HCBFG procedure will be described in section 2

The suggested HCBFG will maintain all the advantages of the high accuracy and CPU efficiency of the body-fitted curvilinear structured grid, and at the same time achieve the flexibility and automation of the Cartesian grid methods in handling complex geometry. The high fidelity schemes for inviscid fluxes and the central differencing scheme for the viscous terms can be employed.

2 The Novel Approach of Hybrid Cartesian Body-Fitted Grid

2.1 General Description

The novel hybrid Cartesian body-fitted grid strategy can be implemented by the following steps:

1) Generate a background Cartesian grid covering the entire computational domain (including any embedded bodies) with the grid spacing of Δ_t. Fig. 1 shows an example, in which the thick solid line is the solid surface boundary of an embedded body. The circle points define the shape of the solid body geometry.

2) Determine the near wall boundary (NWB), which will have nearly the same distance from the solid surface everywhere and the similar shape to the geometry. Fig. 2 demonstrates an example of the NWB of the HCBFG for a circular cylinder, which is generated using the proposed strategy. The solid mesh lines in Fig. 2 are the body-fitted grid within the NWB. The background Cartesian grid lines are shown as dotted lines. The detailed procedure of the NWB search and the body-fitted-grid (BFG) generation will be described separately in next section.

3) Once the NWB is determined, the BFG can be generated within it straightforwardly. The background CG is used to generate the grid lines in the circumferential direction. They are either the horizontal, vertical or the diagonal lines from the intersecting points of the CG with the NWB. The only mesh lines that need to be generated by the algebraic method within NWB are those tangential to the solid body surface. Since the NWB is very close to the wall surface and only the mesh lines tangential to the wall surface need to be generated, a simple algebraic method can generate a high quality stretched grid. The grid line skew angle β is guaranteed mathematically in the range $45^\circ \le \beta \le 135^\circ$. The skew angle β is defined as the angle between any two grid lines. In this way, all the grid points on the NWB are connected to the background CG as shown in Fig. 2 and hence no interpolation is needed.

In general, the HCBFG methodology can be applied to any irregular geometry as long as the background CG is fine enough to resolve the shape of the solid boundary geometry. If a geometry system has a large variation of the geometry length scales, a local refinement of the background CG can be used for the small scale geometry.

2.2 Search the Near Wall Boundary for Body-Fitted Grid

Obviously, the procedure described above indicates that the most important step is Step 2): Determine the NWB. The near wall boundary is formed by the three types of grid lines from the background CG, horizontal, vertical and 45° diagonal lines of CG cells. The distance difference of any two adjacent points on the NWB from their wall surface intersecting points will not be greater than one CG cell. This is to ensure that the NWB has the similar shape and is close to the solid surface so that the wall boundary layer will be sufficiently resolved. The following explains the detailed procedure to determine the NWB using a 2D case as an example.

Step 1:

Global search of the background Cartesian cell location that the 1st wall surface defining point falls in. As shown in Fig. 1, the solid boundary Γ_b is stored and represented in discrete form, namely, wall surface defining points (marked with circles). In this example, those surface defining points are numbered from 1 to 11. The global search can be done by finding the minimum distance of the point 1 to the centroids of all the Cartesian cells. A Cartesian cell and its centroid are book-kept using index numbers (i, j), where i and j indicate the row and column location of the lower left corner node of the cell as shown in Fig. 3. A 2-D Cartesian grid cell has four interfaces and are identified as $S_k(i, j)$, where k is counted counterclockwise from 1 (left segment) to 4 (upper segment) as depicted in Fig. 3.

Step 2:

Search all the intersection points of the wall boundary on the background CG. This search is done one by one through all the wall surface defining points. Locally, a 3rd order polynomial is constructed using 4 wall surface defining points. It is trivial to determine the intersection points of the CG with the wall surface since the CG grid lines are either at constant x or y. Take the case in Fig. 3 as an example, once one intersection point is located such as the square symbol on $S_1(i,j)$, the next intersection point location only has two scenarios, intersecting with cell (i,j) itself or the adjacent $(i-1,j)$ cell that shares the common interface $S_1(i,j)$. Repeat this process until all the intersection points of the CG with the wall surface are found.

Step 3:

Use the wall surface segment connected by two intersection points within each cell of the CG to determine the advancement of the NWB from the wall surface. The NWB advancing direction is determined by the wall surface normal outward pointing vector,

$$\mathbf{n} = A_x\mathbf{i} + A_y\mathbf{j} \tag{1}$$

There are the following five cases for the NWB advancing direction:

1) If $|A_y/A_x| > 1$, and $A_y > 0$, the NWB will advance in positive y-direction (horizontal lines)
2) If $|A_y/A_x| > 1$, and $A_y < 0$, the NWB will advance in negative y-direction (horizontal lines)
3) If $|A_y/A_x| < 1$, and $A_x > 0$, the NWB will advance in positive x-direction (vertical lines)
4) If $|A_y/A_x| < 1$, and $A_x < 0$, the NWB will advance in negative x-direction (vertical lines)
5) Corner cells: The vertical or horizontal lines of NWB need to be connected by the corner cells with 45° diagonal lines to surround a solid surface. The cases 1) - 4) will be checked for each intersecting point of the CG with the solid wall surface. When the vertical or horizontal distance of two adjacent NWB points is greater than one CG cell, it must be in the corner region and the mesh needs to be turned. The corresponding solid surface segment with $|A_y/A_x|$ closest to 1.0 will be used as the corner point and its original NWB advancement in either x- or y- direction will be discarded. A 45° diagonal line then will be used to connect the two neighboring points of the NWB.

For cases 1) - 4) above, the advancing distance of the NWB is determined by the number of the complete CG cell segments that the NWB must include. We use ib to stand for the number of the complete CG cell segments. Fig. 4 shows the cases that ib=1 and 2. In other words, the thickness of NWB is controlled by ib. The NWB corresponding to the corner cells is formed by connecting the two adjacent points of the NWB and it naturally goes through the diagonal lines of the CG. This procedure ensures that all the grid skew angle β falls between $45° \leq \beta \leq 135°$ to have high a quality mesh. For the corners cells inside the NWB, a diagonal grid line introduced from the background CG is usually added to maintain a uniform grid density in the circumferential direction.

There is another situation that a 45° diagonal line will be used. It is when the two adjacent NWB segments have the same slope (0° or 90°), but the distance is one CG cell. Then the two segments will be connected by a 45° diagonal line naturally.

The CG cells adjacent to a 45° diagonal line will be right-angled isosceles triangle cells (2D) or prism with right-angled isosceles triangle section (3D). These triangle cells do not create difficulties for a structured grid solver. If a finite volume method is used, there is no difficulty to calculate the volume and surface flux. If a finite difference method is used, the triangle cells nodes can be just treated as regular inner grid points because they are connecting the mesh within the NWB and the Cartesian grid.

Step 4:

Check all the grid cells within the NWB to see if there is any triangle element, which may occur for two body intersection. The triangle elements can be easily converted to tetrahedral cells by discarding one adjacent grid line from the background CG.

2.3 Extension to 3D

An appealing advantage of the HCBFG is that the strategy developed for the 2D mesh can be straightforwardly extended to 3D. This is attributed to the background CG that is used as a common communicator and location reference for each individual grid block. Again, the 3D BFG will be generated based on the background 3D CG. The NWB will be also advanced based on the direction of outward pointing normal vector of the wall surface intersection with the CG, which can be calculated by the cross product of the two diagonal line vectors of a surface. For most 2-D cases, the wall boundary can be well covered by a structured one-block body fitted grid. However, for 3-D cases, multi-blocks of the body fitted grid system may be necessary depending on the surface curvature variation.

2.4 Some HCBFG Examples

Fig. 2 is the mesh for a HCBFG of a circular cylinder, which has been used as an example to explain the methodology. The *ib* for this grid is 1. Fig. 5 is the HCBFG of RAE2822 airfoil with the *ib* value equal to 1. The BFG in this case surrounds the solid surface. To resolve the wake gradient, an imaginary boundary is added along the centerline of the wake and the refined mesh in the wake region can be easily generated as shown in Fig. 16. Fig. 6 shows a hybrid Cartesian-body fitted grid system for flow past a L-shape block. This example indicates that the method can handle the 90-degree corners very well. The control parameter *ib* is convenient to control the thickness of the NWB according to the estimated boundary layer thickness. Fig. 5 also indicate that the HCBFG methodology can handle a sharp trailing edge very well.

The procedure is directly extended to 3D and a HCBFG is generated for a 3D sphere. Fig. 7 shows the HCBFG, which has the H-type grid on the poles and the O-type grid around the central section. The H-type grid on the poles have been moved apart from the sphere surface to give an inside view. Fig. 8 is the center cross section of the sphere showing the O-mesh around the surface.

To mimic the situation of wing-fuselage intersection or control surface-fuselage intersection, the HCBFG is applied to generate the mesh for two intersecting 3D cylinders with different diameters. The intersecting line formed between the two cylinders is a 3D curve. This is not trivial for a conventional structured grid generation due to the intersection of the mesh. However, it is fairly straightforward for the HCBFG methodology. The two individual NWB mesh surrounding each cylinder is generated first. Then based on the common boundary determined by the background CG, let the two NWB intersect by removing the mesh cells on the surface of the larger cylinder. Again, using the same *ib* number for both surface, the two mesh can be connected by the 45° diagonal lines. Fig. 9 shows the 3D mesh of the two intersecting cylinders. To make it clear to see, only one layer of the CG on the cross section is shown. Fig. 10 shows the surface mesh of the two intersecting cylinders. Again, all the 3D grid line skew angles are between 45° and 135° and all the grid cells within the NWBs are hexahedrons. All the grid points between the NWBs and the background Cartesian grid are one-to-one connected.

3 Flow Governing Equations

The governing equations for the flow field computation are the Reynolds-Averaged Navier-Stokes equations (RANS) with Favre mass average which can be transformed to the generalized coordinates and expressed as:

$$\frac{\partial \mathbf{Q}'}{\partial t} + \frac{\partial \mathbf{E}'}{\partial \xi} + \frac{\partial \mathbf{F}'}{\partial \eta} + \frac{\partial \mathbf{G}'}{\partial \zeta} = \frac{1}{Re}\left(\frac{\partial \mathbf{E_v}'}{\partial \xi} + \frac{\partial \mathbf{F_v}'}{\partial \eta} + \frac{\partial \mathbf{G_v}'}{\partial \zeta}\right) \tag{2}$$

where Re is Reynolds number and

$$\mathbf{Q}' = \frac{\mathbf{Q}}{J} \tag{3}$$

$$\mathbf{E}' = \frac{1}{J}(\xi_t \mathbf{Q} + \xi_x \mathbf{E} + \xi_y \mathbf{F} + \xi_z \mathbf{G}) = \frac{1}{J}(\xi_t \mathbf{Q} + \mathbf{E}'') \tag{4}$$

$$\mathbf{F}' = \frac{1}{J}(\eta_t \mathbf{Q} + \eta_x \mathbf{E} + \eta_y \mathbf{F} + \eta_z \mathbf{G}) = \frac{1}{J}(\eta_t \mathbf{Q} + \mathbf{F}'') \tag{5}$$

$$\mathbf{G}' = \frac{1}{J}(\zeta_t \mathbf{Q} + \zeta_x \mathbf{E} + \zeta_y \mathbf{F} + \zeta_z \mathbf{G}) = \frac{1}{J}(\zeta_t \mathbf{Q} + \mathbf{G}'') \tag{6}$$

$$\mathbf{E_v}' = \frac{1}{J}(\xi_x \mathbf{E_v} + \xi_y \mathbf{F_v} + \xi_z \mathbf{G_v}) \tag{7}$$

$$\mathbf{F_v}' = \frac{1}{J}(\eta_x \mathbf{E_v} + \eta_y \mathbf{F_v} + \eta_z \mathbf{G_v}) \tag{8}$$

$$\mathbf{G_v}' = \frac{1}{J}(\zeta_x \mathbf{E_v} + \zeta_y \mathbf{F_v} + \zeta_z \mathbf{G_v}) \tag{9}$$

where the variable vector $\mathbf{Q}$, and inviscid flux vectors $\mathbf{E}$, $\mathbf{F}$, and $\mathbf{G}$ are

$$\mathbf{Q} = \begin{pmatrix} \bar\rho \\ \bar\rho\tilde u \\ \bar\rho\tilde v \\ \bar\rho\tilde w \\ \bar\rho\tilde e \end{pmatrix}, \mathbf{E} = \begin{pmatrix} \bar\rho\tilde u \\ \bar\rho\tilde u\tilde u + \tilde p \\ \bar\rho\tilde u\tilde v \\ \bar\rho\tilde u\tilde w \\ (\bar\rho\tilde e + \tilde p)\tilde u \end{pmatrix}, \mathbf{F} = \begin{pmatrix} \bar\rho\tilde v \\ \bar\rho\tilde u\tilde v \\ \bar\rho\tilde v\tilde v + \tilde p \\ \bar\rho\tilde w\tilde v \\ (\bar\rho\tilde e + \tilde p)\tilde v \end{pmatrix}, \mathbf{G} = \begin{pmatrix} \bar\rho w \\ \bar\rho\tilde u\tilde w \\ \bar\rho\tilde v\tilde w \\ \bar\rho\tilde w\tilde w + \tilde p \\ (\bar\rho\tilde e + \tilde p)\tilde w \end{pmatrix},$$

The $\mathbf{E}''$, $\mathbf{F}''$, and $\mathbf{G}''$ are the inviscid fluxes at the stationary grid system and are:

$$\mathbf{E}'' = \xi_x \mathbf{E} + \xi_y \mathbf{F} + \xi_z \mathbf{G},$$

$$\mathbf{F}'' = \eta_x \mathbf{E} + \eta_y \mathbf{F} + \eta_z \mathbf{G},$$

$$\mathbf{G}'' = \zeta_x \mathbf{E} + \zeta_y \mathbf{F} + \zeta_z \mathbf{G},$$

and the viscous flux vectors are given by

$$\mathbf{E_v} = \begin{pmatrix} 0 \\ \bar\tau_{xx} - \overline{\rho u''u''} \\ \bar\tau_{xy} - \overline{\rho u''v''} \\ \bar\tau_{xz} - \overline{\rho u''w''} \\ Q_x \end{pmatrix}, \mathbf{F_v} = \begin{pmatrix} 0 \\ \bar\tau_{yx} - \overline{\rho v''u''} \\ \bar\tau_{yy} - \overline{\rho v''v''} \\ \bar\tau_{yz} - \overline{\rho v''w''} \\ Q_y \end{pmatrix}, \mathbf{G_v} = \begin{pmatrix} 0 \\ \bar\tau_{zx} - \overline{\rho w''u''} \\ \bar\tau_{zy} - \overline{\rho w''v''} \\ \bar\tau_{zz} - \overline{\rho w''w''} \\ Q_z \end{pmatrix}$$

In above equations, ρ is the density, u, v, and w are the Cartesian velocity components in x, y and z directions, p is the static pressure, and e is the total energy per unit mass. The overbar denotes the Reynolds-averaged quantity, tilde and double-prime denote the Favre mean and Favre fluctuating part of the turbulent motion respectively. All the flow variable in above equations are non-dimensionlized by using the freestream quantities and reference length L.

Let subscript 1, 2 and 3 represent the coordinates, x, y, and z, and use Einstein summation convention, the shear-stress and Q_x, Q_y, Q_z terms in non-dimensional forms can be expressed in tensor form as

$$\bar{\tau}_{ij} = -\frac{2}{3}\tilde{\mu}\frac{\partial \tilde{u}_k}{\partial x_k}\delta_{ij} + \tilde{\mu}(\frac{\partial \tilde{u}_i}{\partial x_j} + \frac{\partial \tilde{u}_j}{\partial x_i}) \tag{10}$$

$$Q_i = \tilde{u}_j(\bar{\tau}_{ij} - \overline{\rho u'' u''}) - (\bar{q}_i + C_p\overline{\rho T'' u_i''}) \tag{11}$$

where the mean molecular heat flux is

$$\bar{q}_i = -\frac{\tilde{\mu}}{(\gamma - 1)Pr}\frac{\partial a^2}{\partial x_i} \tag{12}$$

The molecular viscosity $\tilde{\mu} = \tilde{\mu}(\tilde{T})$ is determined by Sutherland law, and $a = \sqrt{\gamma R T_\infty}$ is the speed of sound. The equation of state closes the system,

$$\bar{\rho}\tilde{e} = \frac{\tilde{p}}{(\gamma - 1)} + \frac{1}{2}\bar{\rho}(\tilde{u}^2 + \tilde{v}^2 + \tilde{w}^2) + \bar{\rho}k \tag{13}$$

where γ is the ratio of specific heats, k is the Favre mass-averaged turbulence kinetic energy. The viscosity is composed of $\mu + \mu_t$, where μ is the molecular viscosity and μ_t is the turbulent viscosity determined by Baldwin Lomax model[36]. In the present calculation, the $\bar{\rho}k$ in Eq.(13) is omitted based on the assumption that the effect is small.

In the work presented herein an implicit high fidelity flow solver is used. The flow solver is based on a hexahedral cell-centered, finite volume upwind approach using the Roe scheme[37]. The 3-order accuracy is achieved for the inviscid fluxes by Monotone Upstream-Centered Scheme for Conservation Laws(MUSCL)[38]. The solutions are integrated in time by using the implicit unfactored Gauss-Seidel iteration with local time step.

4 Data Exchange at NWB

The HCBFG method is developed as a multiblock structured grid code in a parallel computer environment. The communication between the Cartesian and the body-fitted grids is implemented by MPI. Figure 11 illustrates the interface between the Cartesian and the body-fitted grids. Each grid boundary cell requires flow variable values from its neighbors in the adjacent grid block. The flow variables can be exchanged using the halo cells at each grid boundary. The number of the layers of the halo cells is determined by the order of accuracy of the numerical scheme to preserve the same order of accuracy as interior cells. As shown in Fig. 11, there are two kinds of boundary cells for Cartesian grid: aligned boundary cell and non-aligned boundary cell. A non-aligned boundary cell is also called corner cell which is cut by the interface in half. All boundary cells from both Cartesian and the body-fitted grids are in one-to-one correspondence relationship across the interface. Consequently, there is no need of using any interpolation procedure, and the conservation law is fully enforced across the interface.

Fig. 12 illustrates the data exchange procedure between the aligned boundary cells. Such data exchange is to update the variables for the halo cells from the corresponding interior cells in the adjacent grid. For the case of non-aligned boundary cells (or corner cell), the flow variables at halo cells for the body-fitted grid can be found in a diagonal direction in the interior domain of the Cartesian grid. In other words, the corner cell and its halo cells can be treated as the way shown in Fig. 13. In physical domain, a corner cell is an isosceles right triangle in 2D, which can not be directly dealt with by the flow solver developed based on quadrilateral/hexahedral grid systems. To bypass this problem, the corner cell can be treated as a regular square cell formed using cell face S_1, S_2, S_3 and S_4 instead of S_1, S_2, and S, and relating the halo cells to the faces S_3 and S_4 instead of S, as shown in Fig. 14. In this way, the regular square cell is equivalent to the triangular cell in calculating the fluxes in the finite volume approach given by Eq. (14).

$$\frac{\partial \bar{\mathbf{Q}}}{\partial t} = -\frac{1}{V}\int_s \mathbf{F}\cdot d\mathbf{s} \tag{14}$$

where $\bar{\mathbf{Q}}$ is the mean values of the solution vector, t is the time, $\mathbf{F} = (F-F_v)\mathbf{i}+(G-G_v)\mathbf{j}+(H-H_v)\mathbf{k}$, and $\mathbf{s}$ is the surface vector enclosing control volume V. Obviously, $\mathbf{F}\cdot\mathbf{S_1}+\mathbf{F}\cdot\mathbf{S_2}+\mathbf{F}\cdot\mathbf{S_3}+\mathbf{F}\cdot\mathbf{S_4} = \mathbf{F}\cdot\mathbf{S_1}+\mathbf{F}\cdot\mathbf{S_2}+\mathbf{F}\cdot\mathbf{S}$ since if $\mathbf{S} = A_x\mathbf{i}+A_y\mathbf{j}$, then $\mathbf{S_3} = A_x\mathbf{i}$ and $\mathbf{S_4} = A_y\mathbf{j}$. Theoretically, $\bar{\mathbf{Q}}$ is located at the center of the triangular cell. In this treatment, $\bar{\mathbf{Q}}$ can be also considered to be at the center of the regular square cell since $\bar{\mathbf{Q}}$ is the mean values over the control volume. The V is the volume of the actual triangular cell.

5 Implicit Gauss-Seidel Line Iteration

In the flow solver, the implicit Gauss-Seidel line iteration is applied in ξ, η, and ζ direction respectively. The solution is updated twice during a complete iteration, once during the forward sweep and once during the backward sweep. For Gauss-Seidel iteration along η direction, the governing equations (2) can written as

$$B^{-}\Delta U^{n+1}{}_{i,j-1,k} + \bar{B}\Delta U^{n+1}{}_{i,j,k} + B^{+}\Delta U^{n+1}{}_{i,j+1,k} = \mathbf{RHS}' \tag{15}$$

where

$$\bar{B} = I + A + B + C \tag{16}$$

$$\mathbf{RHS}' = \mathbf{RHS}^n - A^{-}\Delta U^{n+1}{}_{i-1,j,k} - A^{+}\Delta U^{n+1}{}_{i+1,j,k} - C^{-}\Delta U^{n+1}{}_{i,j,k-1} - C^{+}\Delta U^{n+1}{}_{i,j,k-1} \tag{17}$$

where A, B and C are Jacobian coefficient matrices, I is the identity matrix, $\mathbf{RHS}$ is the right hand side of the governing equations, ΔU is the increment of $\bar{\mathbf{Q}}$, and the superscripts n and $n+1$ denote two sequential time steps.

In body-fitted grid, Eq. (15) is formed by looping the j index from the starting point j=1 to the ending point $j = jl$. The solution values at halo cells ($j < 1$ or $j > jl$) are provided either by boundary conditions or the neighbors in the adjacent Cartesian grid. In the Cartesian grid, the solver needs to skip the regions occupied by the body-fitted grid as shown in Fig. 15. For example, jl is 400, and cells between j=195 and j=205 are covered by the body-fitted grid for a particular i. Consequently, Eq. (15) is solved from j=1 to j=194, and then from j=206 to $j = jl$. The solution values at halo cells ($j < 1$ or $j > jl$) come from boundary conditions imposed in the lower and upper boundaries. The solution values at halo cells ($j > 194$ and $j < 206$) are provided by the neighbors in the adjacent body-fitted grid. The starting and the ending indexes are predetermined, and need to be updated after each time step in case of solving a moving grid problem.

6 Results and Discussion

The steady state solution of the transonic RAE 2822 airfoil will be the test case of the HCBFG approach. The freestream conditions for this study are listed in Table 1 below:

Table 1: Free-stream conditions for RAE 2822 Airfoil

Mach	Static Pressure (psia)	Temperature (R)	Angle-of-Attack (deg)	Re
0.729	15.8073	460.0	2.31	6.5×10^6

The turbulent Reynolds stress and heat flux are calculated by the Baldwin-Lomax algebraic model [36]. The airfoil has an unit chord length and is located at the origin of the Cartesian coordinate system. This case is run using a C-type body-fitted grid with 690 cells in circumferential direction (90 cells around the airfoil) and 30 cells in radial direction, and a 13 units×10 units rectangular Cartesian grid with 520 cells in streamwise direction and 400 cells in transverse direction. The farfield boundaries extend to 5 chords from the center of the airfoil in transverse direction, 8 chords from the center of the airfoil in downstream direction. The hybrid grid system is shown in Fig.16. The experimental data of [39] are used for comparison.

The $Mach$ contours is plotted in Fig.17, which shows that the data exchange across NWB works well. The comparison of pressure coefficient on the airfoil is shown in Figure 18. A very good agreement between the computation and experiment is obtained on the pressure surface of the airfoil. There appears to be a discrepancy for the shock location on the suction surface of the airfoil. This discrepancy may be mainly attributed to the insufficient grid resolution in circumferential direction of the airfoil and the relatively small farfield boundary used. In Ref.[2], the baseline model uses 256 grid cells along the same airfoil surface to resolve the shock, and a farfield boundary located 15 chords away from the center of the airfoil. A cure for the resolution problem is to increase the number of grid cells in circumferential direction in the body-fitted grid. To resolve the farfield boundary problem, a coarse grid must be used in the farfield where flow variable gradients are small. A conservative flux treatment is necessary. The work implementing conservative fluxes at different Cartesian mesh boundaries with different grid density is the next step. Figure 19 shows the convergence history of the maximum L_2 norm residual over all the grid points versus iteration number.

7 Conclusion

A novel approach of automated hybrid Cartesian-body fitted grid for simulations of fluid flows in complex geometries has been developed. The transonic RAE2822 airfoil is calculated using an implicit line Gauss-Seidel iteration to demonstrate the feasibility of the method. The computational result agrees well with the experiment. The proposed HCBFG strategy has the following advantages, which are crucial for high fidelity high Reynolds number flow and fluid-structural interaction simulations:

1) All the grid points between the body-fitted grid and the background Cartesian grid are one-to-one connected and no interpolation is needed.
2) All the grid line skew angles β will be in the range $45^\circ \leq \beta \leq 135^\circ$, which ensures a good quality structured grid.
3) All the high order schemes and implicit line relaxation algorithms developed for structured grids can be used to achieve high order accuracy and high CPU efficiency.
4) The stretched body fitted grid can resolve the wall boundary layer of a high Reynolds number flow and hence an economic grid size can be used.
5) The wall boundary conditions can be accurately imposed.
6) The grid generation of a complex moving geometry is significantly simplified and is very efficient due to using an algebraic method. This feature is very important for moving grid and fluid-structural interaction simulations in which the grids need to be updated after every time step.

The grid coarsening procedure for the regions with small gradient far away from walls is necessary to save CPU resource.

8 Acknowledgment

The support from Miami $Wind^{TM}$ is greatly appreciated.

References

[1] X.-Y. Chen, G.-C. Zha, and M.-T. Yang, “Numerical Simulation of 3-D Wing Flutter with Fully Coupled Fluid-Structural Interaction,” *Journal of Computers & Fluids*, vol. 36, No. 5, pp. 856–867, 2007.

[2] X.-Y. Chen, G.-C. Zha, and Z.-J. Hu, “Numerical Simulation of Flow Induced Vibration Based on Fully Coupled-Structural Interactions.” AIAA Paper 2004-2240, AIAA 34th AIAA Fluid Dynamics Conference,, Jaun 28 - July 1, 2004.

[3] X.-Y. Chen and G.-C. Zha, “Fully Coupled Fluid-Structural Interactions Using an Efficient High Resolution Upwind Scheme,” *Journal of Fluids and Structures*, vol. 20, pp. 1105–1125, 2005.

[4] R. B. Melville, S. A. Morton, and D. P. Rizzetta, “Implementation of a Fully-Implicit, Aeroelastic Navier-Stokes Solver.” AIAA Paper-97-2039, 1997.

[5] M. Visbal and D. Rizzetta, “Large Eddy Simulation on Curvilinear Grids Using Compact Differencing and Filtering Schemes,” *Journal of Fluids and Engineering*, vol. 124, pp. 836–847, 2002.

[6] R. Gordnier and R. Melville, “Physical Mechanisms for Limit-Cycle Oscillations of a Cropped Delta Wing.” AIAA Paper 99-3796, 1999.

[7] R. E. Gordnier, “Computation of limit-cycle oscillations of a delta wing,” *Journal of Aircraft*, vol. 40, 2003.

[8] Steger, J. L., Dougherty, F. C. and Benek, J. A., “ A Chimera Grid Scheme.” dvances in Grid Generation, K. N. Ghia and U. Ghia, eds., ASME FED-Vol., June, 1983.

[9] Benek,J. A. ;and Steger,J. L. and Dougherty,F. C. and Buning,P. G. , “ Chimera. A Grid-Embedding Technique.” Final rept. 1 Nov 80-1 Oct 85, APR 1986.

[10] Steger, J.L., “ The Chimera Method of Flow Simulation.” Workshop on Applied CFD, University of Tennessee Space Institute, August 1991.

[11] D. P. Rizzetta and M. R. Visbal, “Numerical Simulation of Separation Control for a Highly-Loaded Low-Pressure Turbine .” AIAA-2004-2204, 2004.

[12] D. Rizzetta and M. Visbal, “Large Eddy Simulation of Supersonic Cavity Flowfields Including Flow Control,” *AIAA Journal*, vol. 41, pp. 1452–1462, 2003.

[13] Chan, W. M. and Rogers, S. E. and Nash, S. M. and Buning, P. G. and Meakin, R. L. and Boger, D. A. and Pandya, S. , “ Chimera Grid Tools User’s Manual, Version 2.0.” http://people.nas.nasa.gov/ wchan/cgt/doc/man.html, July, 2007.

[14] Morton, S. and Tomaro, R. and Noack, R., “ An Overset Unstructured Grid Methodology Applied to a C-130 with a Cargo Pallet and Extraction Parachute .” 44th AIAA Aerospace Sciences Meeting and Exhibit, Reno, Nevada, Jan. 9-12, 2006.

[15] Pandya, M. J. and Frink, N. T., “Agglomeration Multigrid for an Unstructured-Grid Flow Solver.” AIAA 2004-0759, Jan., 2004.

[16] Pandya, M. J. and Frink, N. T. and Noack, R.W, “Progress Toward Overset-Grid Moving Body Capability for USM3D Unstructured Flow Solver.” AIAA 005-5118, Jan., 2005.

[17] Qiu JX, Khoo BC, Shu CW, “A numerical study for the performance of the Runge-Kutta discontinuous Galerkin method based on different numerical fluxes,” *Journal of Computational Physics*, vol. 212, pp. 540–565, 2006.

[18] Luo, H. and Bauma, J. D. and Lhner, R., “A Hermite WENO-based limiter for discontinuous Galerkin method on unstructured grids,” *Journal of Computational Physics*, vol. 225, pp. 686–713, 2007.

[19] Wang, Z. J., “Spectral (finite) volume method for conservation laws on unstructured grids: basic formulation,” *Journal of Computational Physics*, vol. 178, pp. 210 – 251, 2002.

[20] Harris, R. and Wang, Z.J. and Liu, Y., “Efficient Quadrature-Free High-Order Spectral Volume Method on Unstructured Grids: Theory and 2D Implementation,” *Journal of Computational Physics*, vol. 227, pp. 620–1642, 2008.

[21] Mittal, R. and Iaccarino, G., “Immersed Boundary Methods,” *Annual Review of Fluid Mechanics*, vol. 37, pp. 239–261, 2005.

[22] C. S. Peskin, “Flow Patterns Around Heart Valves: A Numerical Method,” *Journal of Computational Physics*, vol. 10, pp. 252–271, 1972.

[23] Mohd-Yusof, J. , “ Combined immersed boundaries/B-Splines Methods for Simulations of Flows in Complex Geometries.” CTR Annual Research Briefs, NASA Ames/Stanford University, pp317-327 , 1997.

[24] Fadlun, E.A. and Verzicco, R. and Orlandi, Mohd-Yusof, J., “Combined Immersed-Boundary/Finite-Difference Methods for Three-Dimensional Complex Flow Simulations,” *Journal of Physics Review*, vol. 161, pp. 35–60, 2000.

[25] Choi, J.-I and Oberoi, R. C. and Edwards, J. R. and Rosati, J. A. , “An Immersed Boundary Method for Complex Incompressible Flows,” *Journal of Computational Physics*, vol. 224, pp. 757–784, 2007.

[26] Cho, Y. and Chopra, J. and Morris, P. J. , “Immersed Boundary Method for Compressible High-Reynolds Number Viscous Flow around Moving Bodies.” AIAA 2007-0125, 45th AIAA Aerospace Sciences Meeting and Exhibit, Reno, Nevada, Jan. 8-11, 2007.

[27] Clarke, D. and Salas, M. and Hassan, H., “Euler Calculations for Multi-Element Airfoils Using Cartesian Grids,” *AIAA Journal*, vol. 24, pp. 1128–35, 1986.

[28] Udaykumar, HS and Shyy, W and Rao, MM , “A Mixed Eulerian-Lagrangian Method for Fluid Flows with Complex and Moving Boundaries,” *Int. J. Numer. Methods Fluids*, vol. 22, pp. 691–705, 1996.

[29] Udaykumar, HS and Mittal, R and Shyy, W. , “Computation of Solid-Liquid Phase Fronts in the Sharp Interface Limit on Fixed Grids,” *Journal of Computational Physics*, vol. 153, pp. 534–74, 1999.

[30] Udaykumar, HS and Mittal, R and Rampunggoon, P. , “A Sharp Interface Cartesian Grid Method for Simulating Flows with Complex Moving Boundaries,” *Journal of Computational Physics*, vol. 174, pp. 345–80, 2001.

[31] Udaykumar, HS and Mittal, R and Rampunggoon, P. , “Interface Tracking Finite Volume Method for Complex Solid-Fluid Interactions on Fixed Meshes,” *Commun. Numer. Methods Eng.* , vol. 18, pp. 89–97, 2002.

[32] M. Berger, M. Aftosmis, and J. Melton, “Accuracy, adaptive methods and complex geometry.” Proc. First AFOSR Conference on Dynamics Motion CFD, 1996.

[33] M. Berger, H. C., and R. Leveque, “H-Box Methods for the Approximation of Hyperbolic Conservation Laws on Irregular Grids,” *SIAM Journal on Numerical Analysis*, vol. 41, pp. 893–918, 2003.

[34] H. C., M. Berger, and R. Leveque, “A High-Resolution Rotated Grid Method for Conservation Laws with Embedded Geometries,” *SIAM Journal on Scientific Computing*, vol. 26, pp. 785–809, 2005.

[35] M. Berger, “On Conservation at Grid INterfaces.” ICASE Paper No. 84-43, 1984.

[36] B. Baldwin and H. Lomax, “Thin Layer Approximation and Algebraic Model for Separated Turbulent Flows.” AIAA Paper 78-257, 1978.

[37] P. Roe, “Approximate Riemann Solvers, Parameter Vectors, and Difference Schemes,” *Journal of Computational Physics*, vol. 43, pp. 357–372, 1981.

[38] B. Van Leer, “Towards the Ultimate Conservative Difference Scheme, III,” *Journal of Computational Physics*, vol. 23, pp. 263–75, 1977.

[39] P. Cook, M. McDonald, and M. Firmin, “Aerofoil RAE 2822 - Pressure Distributions, and Boundary Layer and Wake Measurements.” AGARD Report AR 138, 1979.

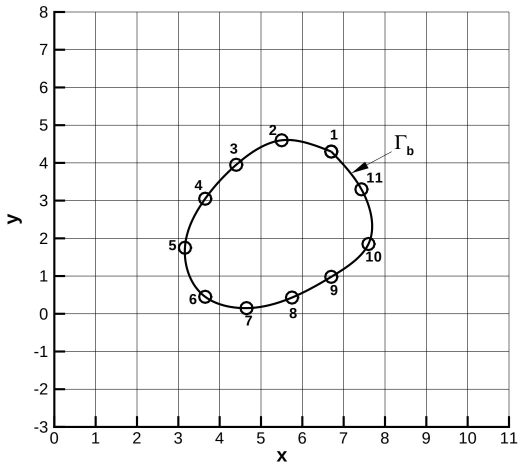

Figure 1: A graphic representation of a solid body embedded in a Cartesian grid.

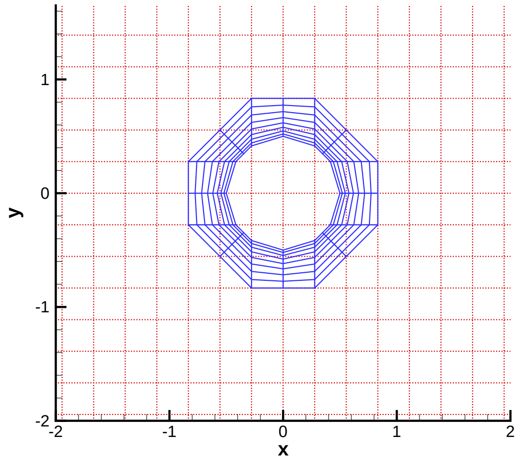

Figure 2: A hybrid Cartesian-body fitted grid for a circular cylinder ($ib = 1$).

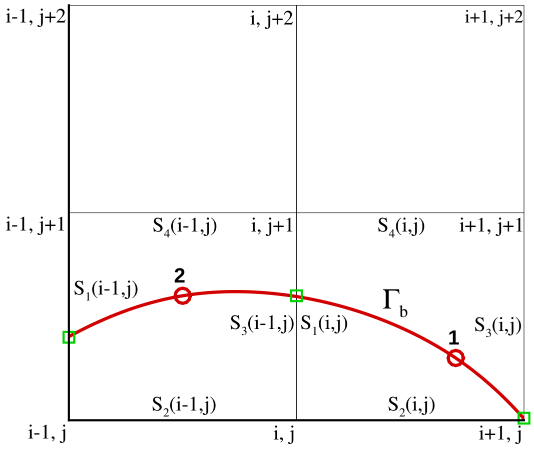

Figure 3: Wall surface intersection with the Cartesian grid.

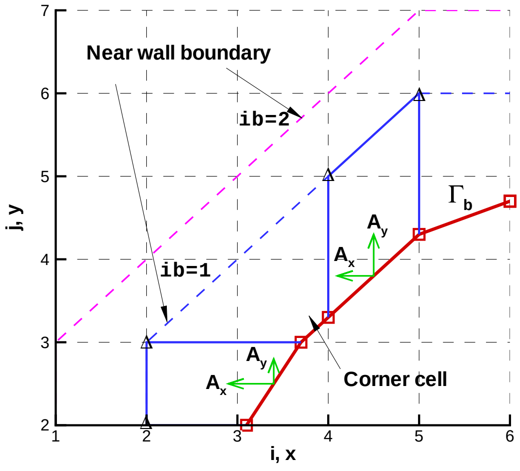

Figure 4: Schematic diagram for advancing the near wall boundary.

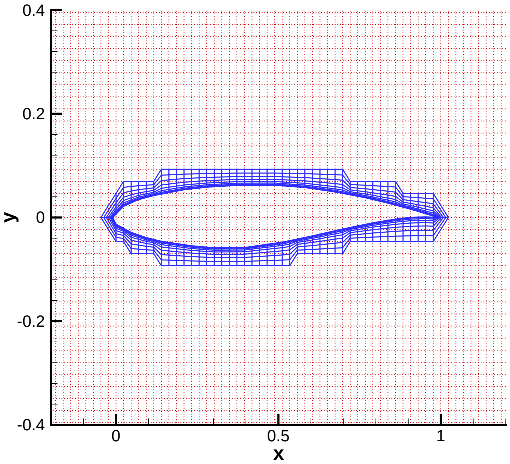

Figure 5: A hybrid Cartesian-body fitted grid for RAE 2822 airfoil ($ib = 1$).

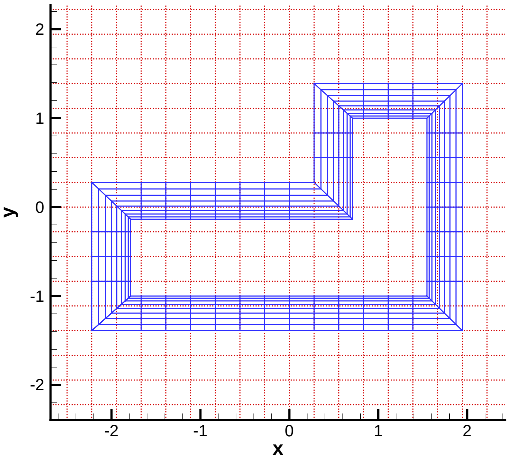

Figure 6: A hybrid Cartesian-body fitted grid system for flow past a L-shape block ($ib = 1$).

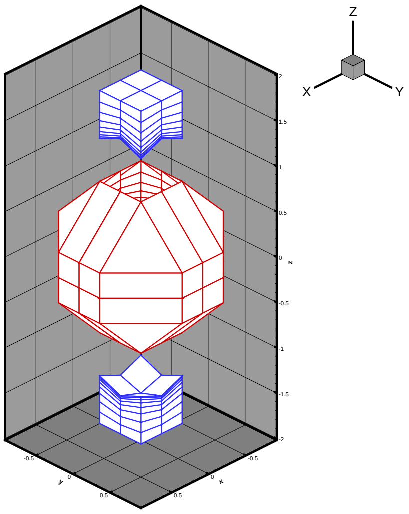

Figure 7: A body fitted grid system around a 3-D sphere: the middle part is covered by an O-type grid, and the poles are covered by two H-type grids which have been moved upwards and downwards from their positions respectively to give an inside view.

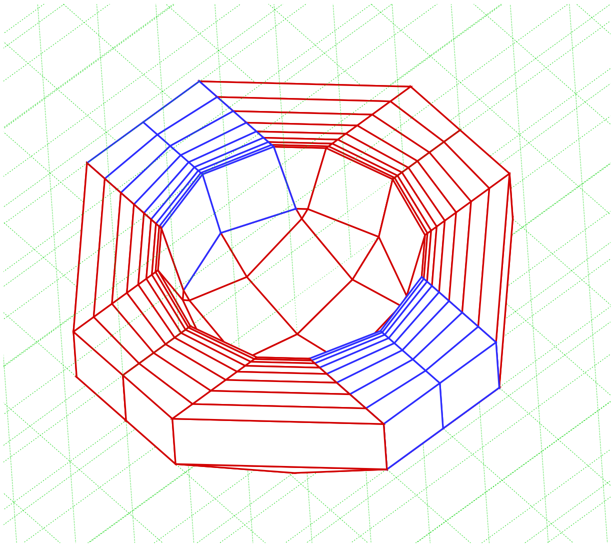

Figure 8: A hybrid Cartesian-body fitted grid system for a 3-D sphere (only half of the grid zone within the NWB is shown).

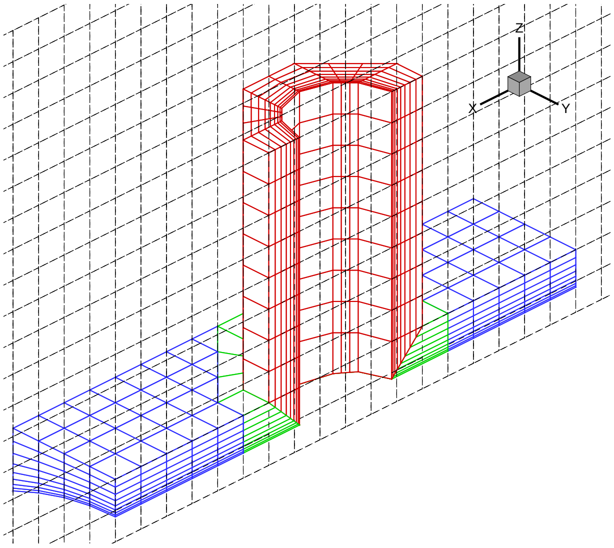

Figure 9: 3D HCBFG for two intersecting cylinders.

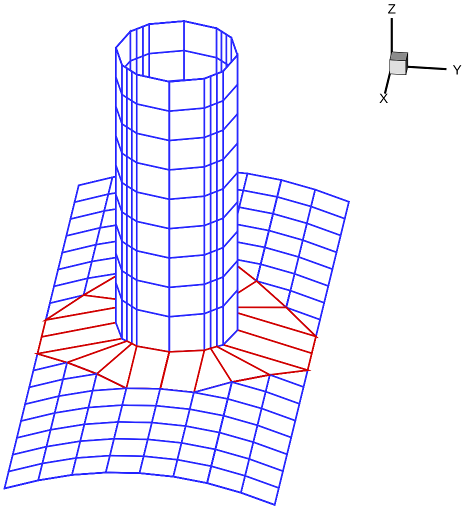

Figure 10: The surface mesh of the two intersecting cylinders.

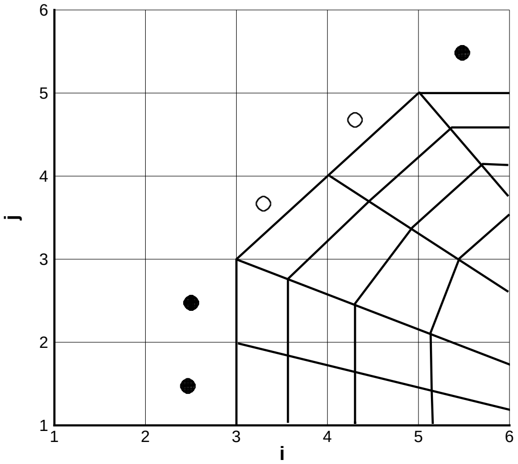

Figure 11: Two kinds of boundary cells for Cartesian grid: aligned boundary cells marked with solid circles and non-aligned boundary cells marked with circles.

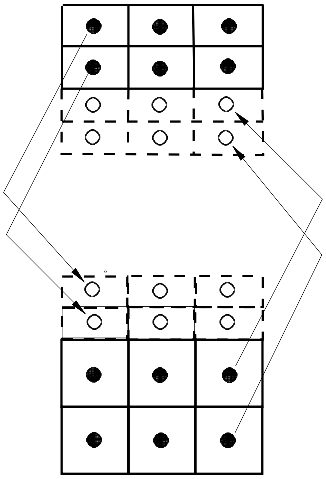

Figure 12: Information exchange procedure between the aligned boundary cells: solid circles denote interior cells and circles denote halo cells.

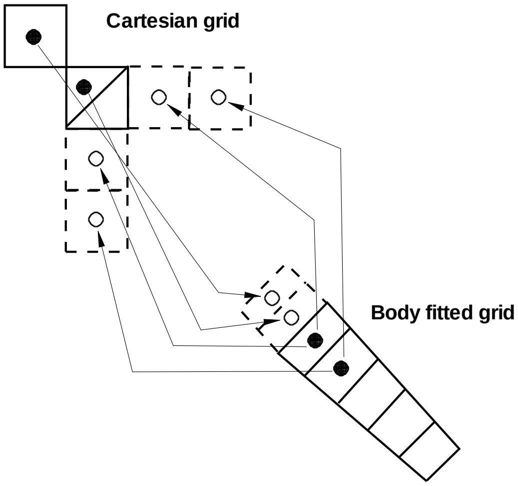

Figure 13: Information exchange procedure between the non-aligned boundary cells: solid circles denote interior cells and circles denote halo cells.

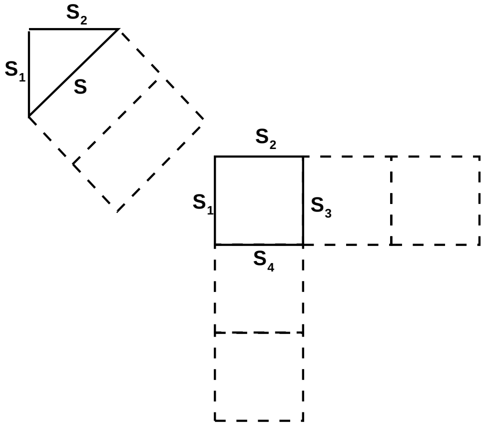

Figure 14: Special treatment for corner cells.

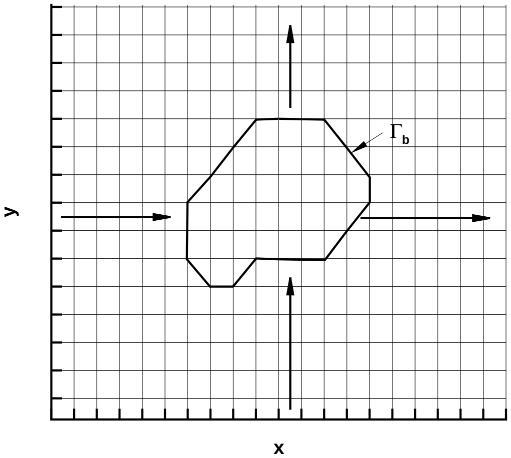

Figure 15: The Gauss-Seidel line iteration in Cartesian grid.

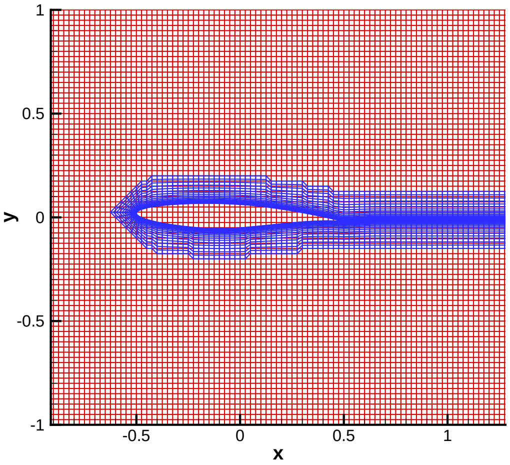

Figure 16: The computational grid system for RAE 2822 airfoil with wake refinement ($ib = 3$).

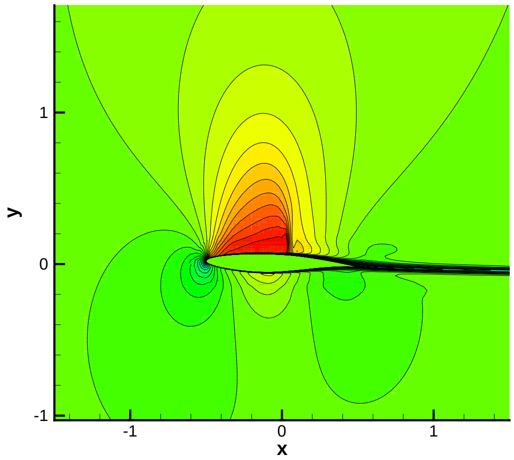

Figure 17: *Mach* number contours for the RAE 2822 airfoil.

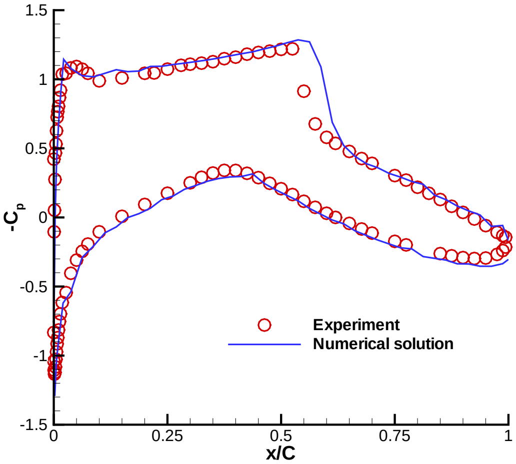

Figure 18: Pressure coefficient distribution compared with the experiment for the RAE 2822 airfoil.

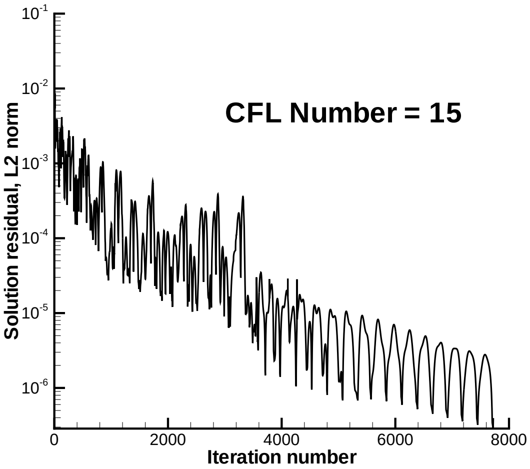

Figure 19: Convergence history.